PHYSICAL REVIEW B **91**, 245308 (2015)

Voltage bistability of coherent electron injection and nonlinear dynamics of a Bloch oscillation in a semiconductor superlattice

C. Minot,[1,2,*] V. S. Jagtap,[2] E. Galopin,[2] J. C. Harmand,[2] S. Barbay,[2] and J. Mangeney[3]
[1]*Institut Mines-Telecom/Telecom ParisTech, 46 rue Barrault, 75 634 Paris Cedex 13, France*
[2]*CNRS/LPN, Laboratoire de Photonique et de Nanostructures, 91 460 Marcoussis, France*
[3]*Laboratoire Pierre Aigrain, Ecole Normale Supérieure, CNRS (UMR 8551), Université P. et M. Curie, Université D. Diderot, 75231 Paris Cedex 05, France*

(Received 11 July 2014; revised manuscript received 26 May 2015; published 12 June 2015)

Voltage bistability is demonstrated at low temperature in a biased unipolar GaAs/AlGaAs superlattice, using a design based on tunneling from a charge reservoir into a Wannier-Stark ladder and competition between nearest and next-nearest neighbor coherent injection channels. The static conduction characteristics are accounted for by a density matrix approach of coherent injection in an inhomogeneous three-level system with resistive load. Electrostatic retroaction on the energy levels is shown to provide an adequate nonlinear feedback mechanism for bistability, as well as for other instability regimes including sustained Bloch oscillation above a retroaction threshold.

DOI: 10.1103/PhysRevB.91.245308 PACS number(s): 73.40.Gk, 05.60.Gg

I. INTRODUCTION

In a biased semiconductor superlattice, electrons injected in a Bloch state initially oscillate at the Bloch frequency, the frequency of the energy quantum they acquire from the field over one superlattice period [1]. They are then scattered and the stationary regime of nonlinear electronic transport arises [2]. On one hand, THz emission relying on Bloch oscillation has been demonstrated thanks to coherent injection of Bloch electrons in bipolar structures, such as p-i-n junctions, by means of ultrashort optical pulses [3–6]. Superlattice Bloch states are excited quasi-instantaneously and well-defined oscillations start. However, the time-resolved experiments show that the Bloch oscillation is damped, and shortly after excitation THz radiation emission dies out. Within the quantum picture, a Bloch state is a superposition of localized eigenstates, the Wannier-Stark states [7,8], which generates coherent quantum oscillations and THz radiation. Electrons optically prepared in a Bloch state fully relax into the stationary Wannier-Stark states after a few coherence times and THz emission ceases. On the other hand, Bloch oscillation has not been observed in unipolar structures despite extensive experimental investigation of nonlinear transport in superlattices, neither with the aid of adequate high-frequency circuitry nor through direct optical excitation as in bipolar structures.

In unipolar devices, miniband conduction and the miniband negative differential velocity are well-established, in agreement with the Esaki-Tsu law, which is derived from both semiclassical and quantum transport [9–11]. In this regime of nonlinear transport that does not involve Bloch oscillations, the coherent oscillatory dynamics is averaged out. However, oscillations of the charge density may be generated owing to the negative differential velocity. High-performance electronic devices such as oscillators and mixers have been developed, up to the millimeter-wave range [12]. They are based on convective instabilities of the electron density [13], with dipolar domain buildup and propagation across a superlattice layer [14]. High-frequency limitations depend on the domain transit time and the ratio g between the domain transit time and the dielectric relaxation time.

In fact, an electronic oscillator based on sustained Bloch oscillation turns out to be out of reach using the usual schemes of ohmic injection of the electrons into a semiconductor superlattice region [15]. The reason is that the coherence time of the Wannier-Stark states (in the picosecond or subpicosecond time scale, depending on the temperature) is an upper limit for the Bloch period and is significantly shorter than the transit times ever achieved in superlattice oscillators ($\sim$7 ps in Ref. [16]). In a Bloch oscillator, the transit time must become smaller than the coherence time in order to minimize the convective instability gain [17], or at least be very significantly reduced in comparison to the superlattice oscillators based on negative differential velocity. An increase of the doping of the superlattice is then required to maintain the condition $g \sim 1$ for dipolar domain instabilities [18–20], but this condition cannot be fulfilled in practice for the resulting current densities lie beyond the breakdown threshold. In addition, in such transit-time devices, the electrons never build by themselves any coherent state through a coherent superposition of Wannier-Stark states and, in contrast to optically excited carriers, their motion cannot generate radiation.

Instead of ohmic injection, resonant tunneling provides a coherent injection mechanism from an injection region into different states of an active region [21]. Such injection schemes have been developed for the electrons in quantum cascade lasers (QCLs) in order to reach population inversion [22]. The latter operate in the infrared, up to the THz range [23]. Let us stress however that tunneling injection plays a role fundamentally different here from the one sought in QCLs. In a QCL, injection aims at concentrating the current into the upper state of the laser transition, while the other accessible states are regarded as parasitic channels. Under vanishing inversion conditions, the gain spectrum takes a dispersive shape [24–27], thus reflecting a stationary transport mechanism based on sequential tunneling between successive Wannier-Stark subbands with transverse momentum exchange [28]. On the

---

[*] christophe.minot@lpn.cnrs.fr

contrary, an electronic oscillator based on sustained Bloch oscillation requires an inversionless injection scheme where an electron is injected into several Wannier-Stark states simultaneously and oscillates in the coherent superposition of the states. These Bloch oscillations may lead to the emission of THz radiation before decoherence damps them [29]. Such an out-of-equilibrium regime is expected to take place when electron transport is faster in the coherent injection channels than in the superlattice miniband, i.e., when the Bloch oscillations in the superposition of states occurs before the stationary transport regime is established in the superlattice.

Here, we investigate a purely electronic injection scheme into two consecutive Wannier-Stark states of a miniband simultaneously. More precisely, electrons from an injector quantum well can competitively tunnel into the far-from-resonance state of the nearest-neighbor well and into the resonant state of the next-nearest-neighbor well [30]. Tunneling into the next-nearest well has been observed previously in superlattices [31], but not into the ground state of the next-nearest well. This is a key point here to generate coherence in the ground states. Nearby resonance, voltage bistability between two current-controlled injection regimes is evidenced experimentally and theoretically. Such a behavior reflects an intrinsic charge instability of tunnel injection, a conduction instability rather than a dielectric instability, in which electronic charge can be coherently transferred back and forth between two wells via a third well—the injector well—in strong interaction with the other two. We then show that, under appropriate charge density and flow conditions, a CW Bloch oscillation can be initiated in the superlattice, in which coherent oscillation is sustained by the coherent tunnel injection of the electrons together with a nonlinear dynamics governed by electrostatic feedback. This is in stark contrast to usual resonant tunneling schemes into a single dominant channel. In a resonant tunneling diode (RTD), the current is switched between two voltage-controlled charge density states and two stable voltage branches due to electrostatic feedback [32], and only the injection mechanism is coherent. THz QCLs are based on the same injection and voltage-control schemes as RTDs, but they have to operate outside the regions of current switching instability. They are much more sensitive to the buildup of field domains than RTDs and their design rather demands special care to suppress parasitic instabilities in order to get controllable and stable lasing effect.

We report on our experimental approach in Sec. II, namely the design and characterization of unipolar injector-superlattice structures for coherent injection. Section III is devoted to the quantum transport model implemented to account for the experimental results. In Sec. IV, we extrapolate our model to slightly more conducting structures to further investigate the nonlinear dynamics in connection with the Bloch oscillation.

II. ELECTRICAL CHARACTERIZATIONS OF COHERENT INJECTION IN A SUPERLATTICE

Implementation of coherent injection into a Wannier-Stark ladder demands the injected electrons to be strongly coupled to the superlattice; otherwise scattering is expected to destroy coherence before injection has significantly occurred. However, coupling strength must be notably smaller than the Bloch energy, so that the perturbation of the Wannier-Stark ladder by coupling remains negligible. This sets definite bounds to the design and investigation of coherent injection in superlattice structures.

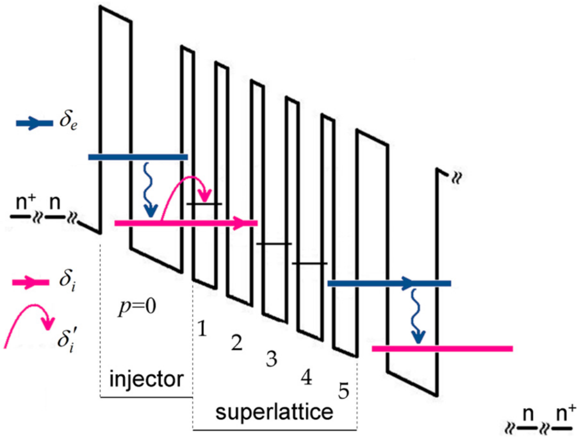

FIG. 1. (Color online) Conduction band diagram at operating bias of next-nearest-neighbor injected superlattice with $N = 5$ coupled quantum wells. Only one basic pattern and an extra injector with its injection and extraction barriers are displayed. δ_i is the resonance splitting of resonant injection into Wannier-Stark state $p = 2$, δ_i' the resonance splitting of nonresonant injection into Wannier-Stark state $p = 1$, and δ_e is the resonance splitting of resonant extraction from Wannier-Stark state $p = 5$. The wavy arrows indicate incoherent relaxation through LO-phonon emission.

A. Structure design

Figure 1 shows a schematic band diagram under negative uniform electric field. Active regions are separated by injection regions. A unit cell of the structure consists of an injector region and a superlattice active region with a constant period. Several unit cells may be stacked, especially for modeling of the electronic structure. The stacking is terminated by an injector sending the carriers into contact layers. In practice, structures with only one unit cell are investigated experimentally here. The active region is a superlattice with N wells, $N - 1$ barriers, and period d ("superlattice" in Fig. 1). The injection and the extraction barriers have thicknesses different from the barrier thickness in the bulk of the superlattice. The superlattice is short enough to push up the transit-time resonance frequency near the Bloch frequency. Due to electron negative differential velocity in the superlattice, transit-time effects take place through the active region and give rise to linear (small-signal) electrical gain around a Hakki resonance, the frequency of which is equal to the inverse of the transit time [10]. The Hakki resonance may generate instable behavior even when $g < 1$, if the impedance of the load circuit compensates the impedance of the device [33]. In fact, the resonance should be located beyond the Bloch frequency to fully ensure that transit-time effects do not play any role. When located nearby the Bloch frequency, enhancement of the charge instabilities by the linear gain is expected, while strict impedance matching remains very unlikely with weakly doped superlattices ($g \ll 1$).

There is only one confined miniband in the active region so that Zener tunneling to higher minibands is minimized. The injector is a wider well than in the superlattice, with two confined levels separated by a LO-phonon energy. In cascaded structures where the basic pattern is repeated, at the design bias, the injector lower level ($p = 0$) is in resonance with the next-nearest-neighbor Wannier-Stark state of the right superlattice, i.e., the second Wannier-Stark state ($p = 2$), and the injector upper level is in resonance with the last ($p = N$) Wannier-Stark state of the left superlattice. In the Fig. 1, with $N = 5$, for Bloch frequency $\nu_{B_0} = 1/T_{B_0} = eF_0d/h$ (e is the electron charge) the voltage drop over one unit cell at the design electric field F_0 is equal to three ($N - 2$) Bloch energies $\hbar\omega_{B_0}$ and a LO-phonon energy $\hbar\omega_{\mathrm{LO}}$, plus half the splitting energies δ_e and δ_i of the extraction and injection tunneling resonances. The resonance splitting energies are associated with the anticrossings of the Wannier-Stark energy levels and characterize the strength of their interaction at and around the resonance [34]. At the design field F_0, the injector lower level is rather far from the resonant tunneling conditions into the first Wannier-Stark state ($p = 1$), which occur near field $2F_0$ with resonance splitting energy δ_i'.

Low n-type doping in each well provides conduction electrons while preventing excessive electron scattering and Joule heating. Due to partial charge transfer to the lowest energy levels at equilibrium, the injector behaves as a charge reservoir where electrons are extracted from a superlattice thanks to resonant extraction (or from the injection contact layers), emit a LO-phonon, then become available for injection into the next superlattice (or into the extraction contact layers).

Similar band engineering has been devised for QCLs [35]. It has not been applied to superlattices for, as explained in the introduction, the design objectives and criteria for QCLs are very different from those of electronic Bloch oscillators. In particular, in a QCL the electrons can reabsorb the photons and cause optical losses. The regular separation of the energy levels in a Wannier-Stark ladder increases losses in the vicinity of the Bloch frequency and is unfavorable for reaching lasing threshold. The electrons also provide cascaded optical gain and, in the THz range, a large number of stages is required to overcome the losses. As a result, THz QCLs are rather thick structures and they are very sensitive to the many different configurations of charge instabilities which may take place inside. For stable operation, the latter have to be eliminated by design as much as possible, considering secondary injection channels as incoherent parasitic channels. On the contrary, in an electronic oscillator based on Bloch oscillation, such channels make it possible to generate coherence between equivalent ground states of a biased regular superlattice, in order to enter an electrical oscillatory regime. The gain and the losses then depend on the electrical environment of the active layers, specifically on the impedance at the oscillation frequency of a suitably designed load antenna, if one is to emit THz radiation into free space [33].

B. Electrical boundary conditions

Transit-time devices may operate under fixed voltage or fixed current boundary conditions. In RTDs [32], large currents can be switched very rapidly because the structures are very short. As a result, current switching only provides small voltage jumps and fixed voltage boundary conditions are suitable for efficient transfer of the generated power to the load circuit.

QCLs differ from the standard transit time devices in the internal engineering of the charge density and the current flow, but they behave similarly regarding field domain formation and the corresponding instabilities, since they also are thick doped devices due to cascading of several active regions. Usually, they satisfy the instability condition $g \sim 1$ at least at the main tunnel resonance where population inversion occurs. As a consequence, they have to operate below that resonance to avoid the field domains, which do not contribute to the optical gain. Again, this is best achieved using a voltage-driven device, i.e., with fixed voltage boundary conditions (see for instance Ref. [35]).

However, inside thick structures, fixed voltage conditions only impose the average field and do not prevent the buildup of field domains. Such conditions are not favorable for Bloch oscillation in short structures with $g \ll 1$; as explained previously, $g \sim 1$ is unrealistic. Electronic Bloch oscillations are charge density oscillations in the longitudinal direction. They generate a retroaction electric field which follows the charge density variations. In short structures with dielectric relaxation time longer than the transit time, fixed voltage boundary conditions impose a large electric field inside the active region externally and hinder the charge density variations [17]. The electronic density cannot follow the rapid changes required for Bloch oscillations. Fixed current boundary conditions which impose no constraint on the internal fields are to be preferred and we chose such conditions in our experiments. Since the electric field in the superlattice may then vary and the Bloch frequency linearly depends on the electric field, the question arises whether steady oscillations at the Bloch frequency may still develop when electrostatic retroaction is taken into account in the Bloch oscillation mechanism. This point will be addressed in more detail in Sec. IV.

C. Sample fabrication and characterization

Four samples with only one repetition of the basic pattern and an extra injector (see Fig. 1) were grown by molecular beam epitaxy. The active region is a GaAs/$\mathrm{Al_{0.15}Ga_{0.85}As}$ superlattice with $d = 9.9$ nm; the wells and barriers are 6.6 nm and 3.3 nm thick, respectively—checked by x-ray diffraction—and $N = 5$. Different injection ($\delta_i = 1{,}3$ meV) and extraction ($\delta_e = 1{,}3$ meV) resonance splittings have been investigated and the samples are denoted by (δ_i,δ_e). Figure 2(a) shows a diagram of the energy levels and their wave functions in sample $(1,1)$ for several repetitions of the unit cell and under uniform electric field F_0 at the design bias $F_0d = 10$ mV. The width Δ of the first miniband of the superlattice is 30 meV. In comparison with Fig. 1, the injector is split into two wells separated by a three-monolayer AlGaAs barrier with reduced Al content. Varying the position of the barrier within the injector and its Al content makes it possible to fine-adjust the level energies, in order to obtain a regular Wannier-Stark ladder and LO-phonon energy separation between the injector upper and lower levels. Each GaAs layer is Si:5×10^{16} cm^{-3} δ-doped over three monolayers at the center.

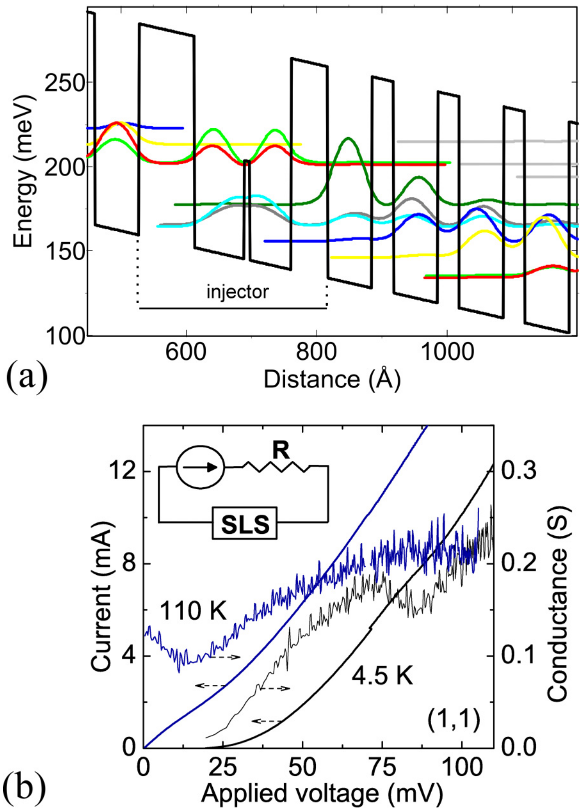

FIG. 2. (Color online) (a) Conduction band diagram of next-nearest-neighbor injected GaAs/Al$_{0.15}$Ga$_{0.85}$As superlattice over one basic pattern of a periodic structure. Moduli-squared wave functions at operating bias $F_0 d = 10$ mV are positioned according to their energy. Injection and extraction resonance splittings are $\delta_i' = 2.8$ meV and $\delta_i = \delta_e = 1$ meV. From left to right, the layer thicknesses are 8.5 nm for the extraction barrier, 7.6/0.9/6.3 nm inside the injector, 5.6 nm for the injection barrier, 6.6 and 3.3 nm for the wells and barriers, respectively, in the five-well superlattice. The Al content of the thin AlGaAs barrier is 7%. (b) Experimental current-voltage characteristics and their derivative for superlattice structure (SLS) ($\delta_i = 1$ meV, $\delta_e = 1$ meV), the band diagram of which is shown in (a), measured at 4.5 K (black) and 110 K (blue). Each GaAs layer is Si:5 × 10^{16} cm^{-3} δ-doped over three monolayers at the center.

The 200 nm thick GaAs buffer layer grown on the n^+-GaAs substrate is Si-doped at 2×10^{18} cm^{-3} and the n^+-GaAs top contact layer is Si-doped at 5×10^{18} cm^{-3}. Gradual doping 50 nm thick transition regions are intercalated between the n^+-GaAs layers and the active layers in order to minimize carrier heating before injection. AuGeNi ohmic contacts are processed on top of rectangular mesas and laterally along their longest side. They are annealed at 420 °C using rapid thermal annealing. The top contact layer is 500 nm thick in order to avoid metal diffusion into the superlattice during annealing. In the current-voltage measurements, the width of the samples is 200 μm and different lengths, 200, 400, and 800 μm, have been investigated. Good proportionality of current to device area is observed over the whole measurement range in the samples with the lowest conductance per unit area, significant deviations from proportionality occurring only in the longest most conducting samples.

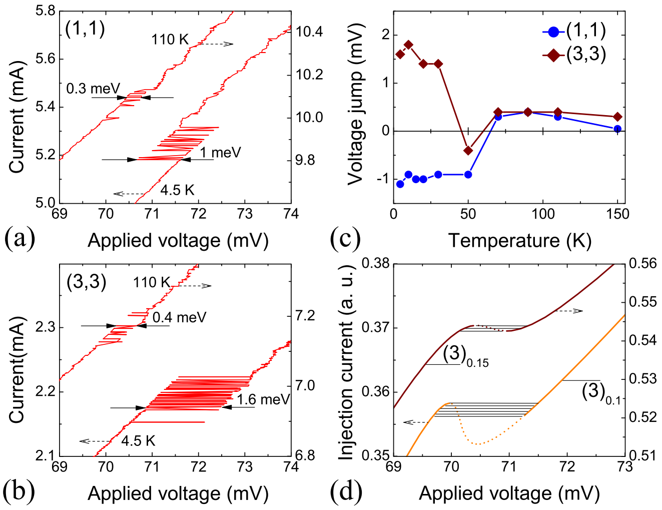

FIG. 3. (Color online) Zooming on current-voltage characteristics at 4.5 K and 110 K in samples (a) (1,1) and (b) (3,3). Device areas are 200 × 200 μm^2. (c) Temperature dependence of voltage jump of bistability. (d) Model detailed in Fig. 5(a) for comparison with (b). The bistability regions are hatched. With injection and extraction couplings δ_i and δ_e, the samples are denoted by (δ_i, δ_e) in the experiments and by $(\delta_i)_{Y_{SL}}$ in the model, where Y_{SL} is the admittance of the load.

The current is measured at low temperature from the voltage drop across a load resistance R ($0.5\ \text{k}\Omega \leqslant R \leqslant 2\ \text{k}\Omega$) much larger than the device resistance. With device capacitance C estimated from the device area and the thickness between the contact layers, the RC time constants are in the range 20–400 ns, much longer than the relaxation times in the semiconductor layers. The current-voltage characteristics of sample (1,1) with 200 × 200 μm^2 area is also shown in Fig. 2(b) at 4.5 K and 110 K. At 4.5 K, the curve exhibits superlinear variation as is expected from resonant tunneling injection. The current is dominated by tunneling through the injector and superlattice barriers. Thermionic emission significantly contributes to the current as temperature is increased, especially at low bias where a linear dependence on applied voltage progressively prevails. A broad resonance is also observed, as evidenced by derivation of the characteristics. In this sample which has the thickest injection and extraction barriers, the resonance is sharp enough to reveal resonant injection to the next-nearest neighbor, with maximum at about 75 mV slightly above the design value (67 mV). The small kink in the characteristics corresponds to a bistable regime which takes place within the resonance, nearby the resonance maximum. This bistable regime also occurs in samples (1,3) and (3,3), while it is not observed in sample (3,1) with smaller extraction/injection splitting ratio. In a small current range, the voltage across the sample switches with a step equal to ΔV and jumps between two different current-voltage curves as the current progressively rises [see Figs. 3(a) and 3(b)]. Invoking Poisson's equation, such a behavior can be attributed to two different charge density states. The voltage switching capacity at nearly constant current then relies upon a charge transfer taking place at the tunnel injection resonance, i.e., into the second Wannier-Stark state. Bistability persists from

4.5 K to about 150 K [see Fig. 3(c)]. The module of ΔV slowly diminishes when temperature increases, but in some devices ΔV cancels and changes sign. Larger values of the magnitude of ΔV—up to 1.8 mV in sample (3,3) at low temperature—are found in the samples with larger extraction and injection couplings.

III. THREE-LEVEL COHERENT INJECTION MODEL

Quantum transport has to be invoked to describe tunnel injection at low temperature in the structures described above. Here, current injection in the superlattice is dealt with in a quantum transport model based on a density matrix approach neglecting in-plane dispersion. Such one-dimensional approximation is valid at low temperature in the real structures, when conduction is mainly governed by resonant transitions near subband minima. Adequate field dependence of the energy levels is required to calculate electrical characteristics, compare them with the experimental data, and validate the model. This is achieved in three steps: first, the electronic structure of one-electron states is obtained under uniform electric field, then the electrostatic retroaction on the energy levels is derived and included in the transport model.

A. Electronic structure and properties

The positions and wave functions of the electronic energy levels in injector/superlattice structures are first obtained from an unperturbed Hamiltonian H_0 for a one-dimensional semiconductor heterostructure under uniform electric field, using an envelope function approximation in a three-band Kane model [36]. Fan charts of the levels as a function of electric field provide the fields where resonance between pairs of levels occurs, as well as the splitting energies δ_i, δ_i', and δ_e [34]. Reduced transition dipoles for injection expressed in units of the superlattice period, u and v, can then be estimated as half the splitting energies, $\delta_i/2$ and $\delta_i'/2$, respectively, divided by the Bloch energy eF_0d, taken as a scaling energy.

Calculation of the wave functions also makes it possible to estimate the decoherence rates. The latter are evaluated below resonance at zero temperature for the LO-phonon interaction (see Table I) [37]. They involve energy conservation conditions (see Fig. 4), so that decoherence of Wannier-Stark states $p = 1$ and $p = 2$ preferentially occurs through interactions with intermediate states $p = 4$ and $p = 5$, respectively. Only the decoherence rates for the lowest transverse momentum values are retained since the other rates involve small Boltzmann factors at low temperature. Decoherence rates between injector and Wannier-Stark states, R_1, R_2, are significantly smaller than decoherence rates R_3 between Wannier-Stark states.

In the following, the Hamiltonian H_0 is restricted to the injector ground state $p = 0$ and two Wannier-Stark states $p = 1,2$ of the superlattice. This is legitimate because the Bloch oscillation amplitude $\Delta/2eF_0$ is $1.5d$ at the operating bias—less than one superlattice period on either side of a well—and the transient dynamics of the injected electrons primarily involves these states. The approximation is strong however since, in particular, forward coupling of state $p = 2$ to downstream states $p > 2$ is disregarded as a coherent mechanism and only dealt with through the boundary conditions. Restriction to only three states enables us to analytically account for the deviations from field uniformity caused by the different charge densities in the wells and to derive a tractable set of nonlinear quantum transport equations.

TABLE I. Main coherence relaxation rates at zero temperature in samples (1,1) and (3,3).

	R_1 (ps^{-1})	R_2 (ps^{-1})	R_3 (ps^{-1})
(1,1)	0.06	$0.05 + 0.09$	1.21
(3,3)	0.23	$0.04 + 0.08$	0.98

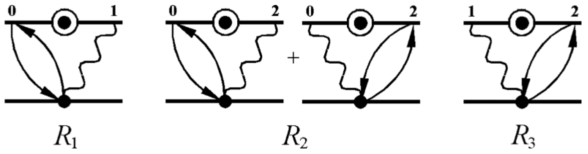

FIG. 4. Main coherence relaxation rates R_1, R_2, and R_3 associated with level pairs (0,1), (0,2), and (1,2), respectively, for electron-phonon interaction in three-level coherent transport. Dots and circled dots refer to interactions involving an intermediate real state and correlations between two states, respectively. The arrows stand for interaction matrix elements, the wavy lines for energy conservation.

B. Electrostatic retroaction

The energy levels in the injector/superlattice structure are localized when an electric field is applied and they are shifted by the electrostatic potential arising from the injected electronic charge density. When the Wannier-Stark states mainly concentrate over their central well [see Fig. 2(a)], such electrostatic retroaction can be obtained from Poisson's equation considering that a field step δF_p is generated by Wannier-Stark state population ρ_{pp} at superlattice wells $p = 1$ and $p = 2$, according to

$$\delta F_p = \frac{en_s}{\varepsilon}\delta\rho_{pp}, \tag{1}$$

where ε is the dielectric permittivity, n_s the charge density per unit area in the injector well, and $\delta\rho_{pp} = \rho_{pp} - \eta_0$ the deviation from equilibrium population η_0.

Integration of Eqs. (1) yields the energy separations $\varepsilon_p - \varepsilon_{p'}$ between all three levels $p,p' = 0,1,2$, $p' \neq p$, as a function of the field, and the sheet density in the injector (see Appendixes A and B); e.g., between states $p = 1$ and $p' = 2$,

$$\varepsilon_1 - \varepsilon_2 = eFd - \frac{e^2n_sd}{\varepsilon}\delta\rho_{22}. \tag{2}$$

In quantum transport, the energy separations are the characteristic frequencies of the coherent dynamics of the electrons injected into the superlattice, up to a factor of h. Here, their linear dependence on the injected electron density itself underpins the electrostatic retroaction effect and the nonlinearity of the coherent dynamics of injection.

From Eqs. (1) and (2), a dimensionless electrostatic retroaction parameter is defined as

$$J = \frac{e^2n_sd}{\varepsilon}\frac{1}{eF_0d}. \tag{3}$$

Its value is proportional to the surface charge density in the injector and depends on the charge transfer into the reservoir. To some extent, J remains an adjustable parameter. If charge transfer is complete, $J \sim 0.43$ for experimental surface charge density in the reservoir $n_s \sim 3 \times 10^{10}$ cm^{-2}.

C. Quantum transport model

The Liouville equation for one-dimensional density matrix ρ is written

$$i\hbar\frac{\partial\rho}{\partial t} = [H_0,\rho] - i\hbar\frac{1}{\tau}(\rho - \overline{\rho}), \tag{4}$$

where $\hbar/\tau$ is the self-energy operator and $\overline{\rho}$ the density matrix in the initial equilibrium state. Equation (4) is used to describe tunnel injection in a three-level extension of the Kazarinov and Suris scheme in the basis of Wannier-Stark states [11,21,34]. The full set of equations is given in Appendix B. For instance, the equations for matrix elements ρ_{21} and ρ_{00} are given as

$$\begin{aligned} i\hbar\frac{\partial\rho_{21}}{\partial t} &= -(eFd - JeF_0d[\rho_{22}-\eta_0] + i\hbar R_3)\rho_{21} \\ &\quad + eFU\rho_{01} - eFV\rho_{20} + i\hbar R_3\overline{\rho}_{21} \\ &\quad - J\frac{\Delta}{4eFd}eF_0d[\rho_{22}-\eta_0](\rho_{11}-\rho_{22}) \end{aligned} \tag{5}$$

and

$$\begin{aligned} i\hbar\frac{\partial\rho_{00}}{\partial t} &= eFU(\rho_{20}-\rho_{02}) + eFV(\rho_{10}-\rho_{01}) \\ &\quad - i\hbar\frac{\rho_{00}-\overline{\rho}_{00}}{T_1} + i\hbar\frac{\rho_{00}^{22}-\overline{\rho}_{00}^{22}}{T_2}. \end{aligned} \tag{6}$$

In Eqs. (5) and (6), $U = ud$ and $V = vd$ are the dipoles for the tunnel transitions from the reservoir to the second and the first Wannier-Stark states associated with splittings δ_i and δ_i', respectively. T_1 and T_2 are the lifetimes in the lower and the upper levels of the injection well. ρ_{00}^{22} stands for the population of the injector upper state.

Transport in the superlattice is accounted for thanks to both initial correlations ($\overline{\rho}_{21} \neq 0$), which is appropriate for the case of homogeneous field, and extra resonant tunneling transfer generated by field inhomogeneity δF obtained from Eq. (A1). As $\Delta/4eF$ is the interaction dipole between Wannier-Stark states $p = 1$ and $p = 2$, the interaction matrix element is

$$e\delta F\frac{\Delta}{4eF} = \frac{en_s}{\varepsilon}\delta\rho_{22}\frac{\Delta}{4F} = \frac{J'}{1+\frac{F-F_0}{F_0}}\delta\rho_{22}eF_0d, \tag{7}$$

where

$$J' = J\frac{\Delta}{4eF_0d}. \tag{8}$$

The total charge is conserved if feeding of the injector lower level by the upper level is taken into account [see Eqs. (B2), (B4), and (B6)],

$$\rho_{00} + \rho_{11} + \rho_{22} = \overline{\rho}_{00} + \overline{\rho}_{11} + \overline{\rho}_{22} + S, \tag{9}$$

with

$$S = \frac{T_1}{T_2}\left(\rho_{00}^{22} - \overline{\rho}_{00}^{22}\right). \tag{10}$$

The current is not calculated self-consistently from the quantum current because the quantum transport model does not extend beyond the second Wannier-Stark state. Instead, a dimensionless injection current equal to the relaxation current from the injector upper level can be defined as eS/T_1 thanks to Eq. (10), assuming that the current injected into the superlattice only flows through fast incoherent relaxation from the upper to the lower level inside the injector. While electron relaxation thus directly gives a fixed current boundary condition at the extraction side of the injector, another boundary condition for the average electric field beyond the injection region is derived from current conservation in the superlattice. For $2 < p \leqslant N$, the average charge density resulting from coherent injection—hence the corresponding resistive part of the load—is kept as an adjustable parameter. Using an ohmic approximation, valid in a small bias range around the bistability region, the electric field in the superlattice for $p > 2$ is taken as

$$F = F_0\frac{SR_{SL}}{N-2}. \tag{11}$$

Ignoring the injection and extraction splittings δ_i and δ_e, the voltage drop across the superlattice and the injector in units of F_0d is written from Eq. (A7) as

$$V_S = SR_{SL} - J(2\rho_{22} + \rho_{11} - 3\eta_0) + \frac{\hbar\omega_{\mathrm{LO}}}{eF_0d}. \tag{12}$$

Equation (12) together with Eqs. (A6)–(A8) include the dependence on the charge density which provides the main basis for the nonlinear dynamics of the voltage across the structure when the static current is fixed. At given electric field F_0 and relaxation time T_1, S is a dimensionless injection current per electron in the reservoir defined as a fraction of current e/T_1, and $R_{SL} = 1/Y_{SL}$ a dimensionless resistance defined as a fraction of resistance F_0dT_1/e. R_{SL} also contains the resistive contributions of the extraction barrier and the superlattice beyond the injection region where a stationary transport regime progressively establishes. In the modeling framework, samples (δ_i,δ_e) are preferably denoted as $(\delta_i)_{Y_{SL}}$, with Y_{SL} reflecting an effective extraction coupling.

D. Voltage bistability of current injection

Competition between the two conduction channels ($0 \rightarrow 1$) and ($0 \rightarrow 2$) arises from population conservation Eq. (9) when the injection current S is a constant. Competition gives rise to nonlinear behavior of the Bloch oscillation involving states $p = 1,2$ when the field is varied around resonance ($0 \rightarrow 2$), i.e., through the resonant tunneling effect between states $p = 0,2$ and the off-diagonal element ρ_{20}, the time derivative of which is governed by

$$\frac{i}{\hbar}[H_0,\rho]_{20} = i\left(\frac{e[F-F_0]d}{\hbar} - J[2\rho_{22}+\rho_{11}]\omega_{B_0}\right)\rho_{20} \tag{13}$$

[the background doping η_0 has been neglected; see Eq. (B3)]. ρ_{20} is a statistical average of coherence which does not randomize to zero in localized states. If an oscillatory regime develops in the system of injected electrons, ρ_{20} oscillates at angular frequency given by the term between parentheses in Eq. (13). Resonant injection does not take place exactly when $F = F_0$, but depends on the charge distribution due to electrostatic retroaction, and generates nonlinear behavior through strong increase of ρ_{22}. Similarly, off-diagonal element ρ_{21} reflects a statistical average of the coherence between Wannier-Stark states $p = 1,2$ giving rise to Bloch oscillation. From Eq. (B1), its time derivative is governed by

$$\frac{i}{\hbar}[H_0,\rho]_{21} = i\left(\frac{eFd}{\hbar} - J\rho_{22}\omega_{B_0}\right)\rho_{21}. \tag{14}$$

The oscillation frequency is thus intimately connected with electrostatic retroaction and the nonlinear dynamics of Bloch oscillation, since the Bloch frequency at field F, $\nu_B = 1/T_B = eFd/h$, is altered by the electrostatic potential originating from injection into the second Wannier-Stark state. J, the electrostatic retroaction parameter for the Wannier-Stark energies, appears as the main feedback parameter of nonlinear coherent dynamics, affecting both the oscillation frequencies of the coherences themselves as in Eqs. (13) and (14) and also, through Eq. (8), their mutual interactions as in Eqs. (B3) and (B5) or their interactions with the populations as in Eqs. (B1), (B4), and (B6). The nonlinearity affecting the oscillation frequencies of the coherences is dominant because $J > J'$ and, principally, because of the resonance effect within a subset of variables, namely ρ_{20}, ρ_{22}, and ρ_{00} and the $(0 \rightarrow 2)$ conduction channel, which makes the system more sensitive to small changes of the injection current.

Such a nonlinear model qualitatively accounts for the experimental observations of voltage bistability in the static regime (see Fig. 3), i.e., the existence of two stable current branches, and voltage switching between the branches within a voltage instability range where a stable current does not exist. Figure 5 shows the stable (solid lines) and unstable (dashed lines) branches of the current-voltage characteristics for $J = 0.15$ (about 35% charge transfer into the reservoir at equilibrium) when coherence relaxation rates and load resistance R_{SL} are varied, for $\delta_i = 1$ meV and $\delta_i = 3$ meV. Each branch and its stability status are calculated thanks to numerical continuation techniques [38]. A multiplicative coefficient r is applied to all rates heuristically to emulate electronic temperature changes. The magnitude of the voltage jump ΔV is reduced when the load resistance R_{SL} is increased (Y_{SL} is reduced), as well as when the coherence relaxation rates are increased using values of coefficient r larger than 1. The bistable behavior eventually vanishes under strong relaxation conditions. Such trends of the model are in agreement with experiments where ΔV diminishes with smaller extraction couplings (smaller Y_{SL}) or at higher temperature (larger r). Semiquantitative agreement is obtained along the voltage scale for samples $(1)_{0.1}$ and $(3)_{0.1}$ at 4.5 K with $r = 1.5$ and $r = 1$, respectively [see Figs. 3(b) and 3(d)]. More qualitative agreement is obtained at 110 K for samples $(1)_{0.15}$ and $(3)_{0.15}$ using a larger value of Y_{SL} than at 4.5 K, with $r = 3$ and $r = 2.2$, respectively.

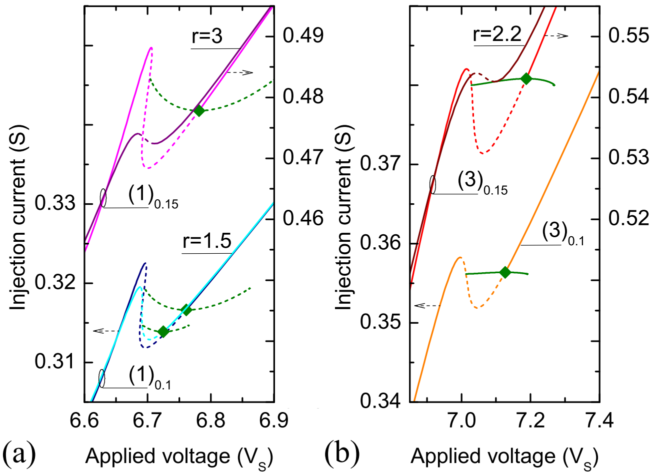

FIG. 5. (Color online) Current-voltage characteristics in the three-level coherent transport model (a) for samples $(1)_{0.1}$ with relaxation coefficients $r = 1$ (dark blue) and $r = 1.5$ (light blue), and $(1)_{0.15}$ with relaxation coefficients $r = 1$ (magenta) and $r = 3$ (purple), (b) for samples $(3)_{0.1}$ with relaxation coefficient $r = 1$ (orange), and $(3)_{0.15}$ with $r = 1$ (red), $r = 2.2$ (dark red). V_S is the voltage drop across one basic pattern (neglecting the splittings δ_i, δ_e), in units of eF_0d. $\delta_i' = 2.8$ meV when $\delta_i = 1$ meV and $\delta_i' = 7.5$ meV when $\delta_i = 3$ meV. Electrostatic retroaction parameter is $J = 0.15$. Unstable branches are shown as dashed lines. Green diamonds and lines are Hopf bifurcation points and voltage oscillation continuations, respectively.

The simulated current-voltage characteristics have not been adjusted on the vertical scale due to intrinsic limitations of the one-dimensional model applied to real structures. The current in Fig. 3(d) is overestimated in comparison with experimental values in the static regime if all electrons in the reservoir only contribute to the coherent current. The overestimation may be attributed to the neglected incoherent relaxation channels, especially to intrasubband scattering in the transverse directions once the electron is in the injector lower level, an effect which, however, does not prevent further coherent injection of the electrons into the superlattice and space charge buildup. The overestimation could be traced to weak efficiency of the direct coherent injection channel between injector and superlattice depicted in Fig. 1. In practice, another cause of discrepancy of the current density between model and experiment may also be the poor adequacy of the model to account for extraction of the electrons from the bulk material contact region into the first injector.

The shift of the resonance when the injection coupling is increased is not clearly observed in the experiments. The model does not explain either why the initial branch may be the lower branch and ΔV may be negative [see Fig. 3(a) at 4.5 K and Fig. 3(c)]. In the plain resonant tunneling mechanism, the upper branch with higher current and lower applied voltage is always the initial branch, because switching first occurs from a higher occupation state when the current or the voltage is increased from below the resonance. Additional tunnel injection and relaxation channels might explain the stabilization of the lower rather than the upper branch below the occurrence of bistability, together with inhomogeneity of the current density in the transverse directions.

Thus, the current-voltage characteristics and voltage bistability observed in the static regime can be explained mainly thanks to tunnel injection with a resistive load and nonlinear feedback effects among the energy levels of the heterostructure. As a result, in contrast to the time-dependent measurements in a linear optical excitation regime, more complex behaviors than plain damping of transients can be expected in the dynamical electrical regime, with the characteristic frequencies showing up in the transport equations, i.e., not only the damping rates but also the coherence oscillation frequencies, especially in the superlattice.

IV. NONLINEAR DYNAMICS OF COHERENT INJECTION

In addition to the current-voltage curves, Fig. 5(a) also shows Hopf bifurcation points marking the onset of nonlinear oscillations, provided injection decoherence (r) is not too large. This means that, in addition to thermal fluctuations, spontaneous oscillations may be responsible for voltage switching. Depending on injection coupling (δ_i), the branch of nonlinear oscillations starting at the bifurcation point can be unstable—with damped oscillations, e.g., in samples $(1)_{0.1}$ and $(1)_{0.15}$ in Fig. 5—or stable with self-sustained nonlinear oscillations, as in samples $(3)_{0.1}$ and $(3)_{0.15}$. In that case, stable oscillations can develop along a branch starting at a supercritical bifurcation, i.e., with amplitude continuously tending to zero as the injection current comes close to the bifurcation point. The oscillation period ranges from at least several Bloch periods nearby the bifurcation point, to very large values near the end of the branch, as expected from nonlinear oscillations. Rich dynamical behavior may take place there with eventually secondary bifurcations and chaotic regimes (not shown in Fig. 5).

Figure 6 displays the electrostatic retroaction dependence of the oscillation period at the Hopf bifurcations. In this diagram, the bifurcation points shown in Fig. 5 are located at abscissa $J = 0.15$ on the thin lines plotted in the top part, with oscillation periods always larger than about three Bloch periods. The diagram shows that the system dynamics is very sensitive to the electrostatic retroaction parameter. In particular, increase of J, i.e., increase of charge transfer into the injector and therefore stronger nonlinearity, brings on extra bifurcations above a retroaction threshold (see thick lines and arrows in Fig. 6). In comparison to the switched voltage ΔV, the threshold exhibits opposite dependence on coherence relaxation rates and load resistance. Noticeably, the frequency of the oscillations may be quite close to the Bloch frequency (within 20%). The closer it is, the smaller the decoherence rates and the larger the injection/extraction couplings are.

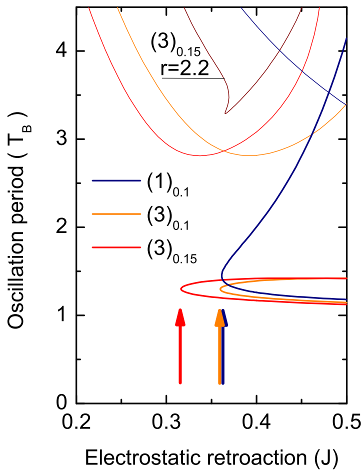

FIG. 6. (Color online) Electrostatic retroaction domains of oscillation period at Hopf bifurcations for samples $(1)_{0.1}$ (blue) and $(3)_{0.1}$ (orange) with $r = 1$, and $(3)_{0.15}$ with $r = 1$ (red) and $r = 2.2$ (dark red).

Above the retroaction threshold, next-nearest-neighbor injection can thus give rise to oscillatory instabilities of the charge density in the superlattice near the resonance frequency of the off-diagonal elements of the density matrix for the Wannier-Stark states, the Bloch frequency. The quantum transport equations in localized states together with Poisson's equation are the ingredients for a semiclassical picture of localized excitations of the charge density in the vicinity of the injector. In analogy with the classical picture of the plasmons, the steady oscillations of the electronic density can be considered as localized plasmons or, more definitely for injector-superlattice structures, localized Bloch plasmon modes [39]. The weak dependence of their frequency on the charge density (J) shows that the electron plasma in and nearby the injector does not screen out the external electric field and Bloch oscillation can be considered as the driving mechanism. An instantaneous Bloch frequency

$$\nu_{B_i} = \frac{eFd}{h} - J\rho_{22}\nu_{B_0} \tag{15}$$

can be defined from Eq. (14). The temporal variations of ν_{B_i} are compensated by the coherent injection terms appearing in the time evolution of the coherence in the superlattice [see Eq. (B1)], so that the oscillation frequency is stabilized slightly below ν_B.

The voltage dependence of the current is displayed in Fig. 7(a) for $J = 0.4$ and sample $(1)_{0.15}$ in both the static and dynamic regimes. The extra Hopf bifurcations are supercritical. When the applied voltage is increased, they are located on the rising edge of the next-nearest-neighbor tunneling

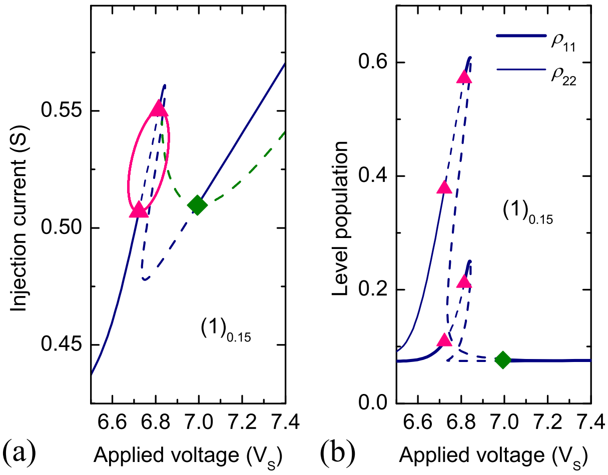

FIG. 7. (Color online) (a) Injection current (blue), (b) nearest (thick blue) and next-nearest (thin blue) neighbor population as a function of applied voltage for sample $(1)_{0.15}$ with $r = 1.5$. Electrostatic retroaction parameter is $J = 0.4$. Hopf bifurcations and voltage oscillation continuations are drawn as green diamonds or pink triangles and green dashed or pink solid lines, respectively. Unstable branches are shown as dashed lines.

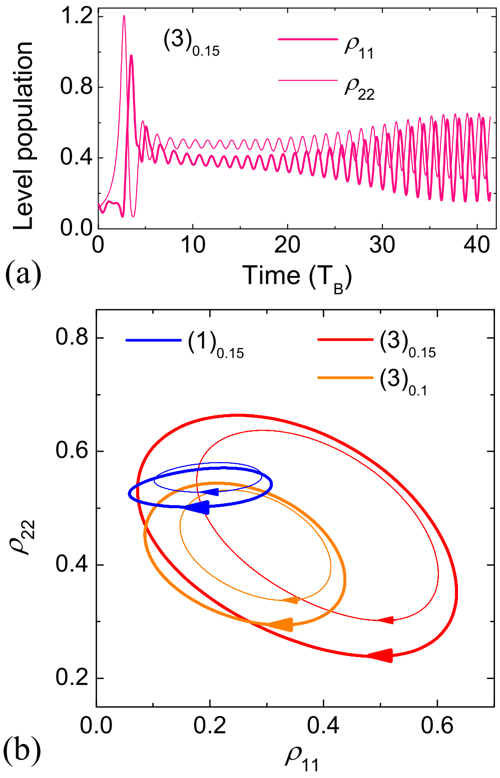

FIG. 8. (Color online) (a) Temporal evolution of the population of the first two Wannier-Stark states from second Hopf bifurcation for sample $(3)_{0.15}$ with $r = 1$. Current is suddenly shifted 10% inside the stable oscillation domain. (b) Parametric plots of asymptotic population trajectories for current suddenly shifted 10% (thin lines) or 20% (thick lines) inside the stable oscillation domain for samples $(1)_{0.1}$ (blue), $(3)_{0.1}$ (orange), and $(3)_{0.15}$ (red) with $r = 1$. Electrostatic retroaction parameter is $J = 0.4$.

resonance [see also Fig. 7(b)]. The temporal evolutions of the populations are depicted in Fig. 8(a) for sample $(3)_{0.15}$ when the current is suddenly shifted from the second bifurcation into the stable oscillation domain. Figure 8(b) summarizes the asymptotic trajectories for samples $(1)_{0.15}$, $(3)_{0.1}$, and $(3)_{0.15}$. They disclose that the oscillatory regime is not a pure Bloch oscillation, in which the variations of the populations of the Wannier-Stark states would be strictly out of phase. This is especially true at low coupling [in sample $(1)_{0.15}$] where the electrons moving back and forth are dominantly transferred into the nearest-neighbor and only a small fraction is sent into the next-nearest Wannier-Stark state in quadrature. For larger coupling, however [e.g., sample $(3)_{0.15}$], the injections are much better equilibrated and mostly out of phase. Their amplitudes decrease with closer proximity to the supercritical bifurcation point, so that steady nonlinear oscillations can develop even with small variations of the electron populations.

The electronic system thus possesses nonlinear longitudinal instabilities of its own with definite frequency nearby the Bloch frequency, quite different from the convective instabilities encountered in transit-time devices. The oscillations can couple to the THz electromagnetic field through spontaneous emission of photons—this is only implicit in our weak-coupling model and hidden in the relaxation rates [29]—or, more usefully, thanks to an external antenna [33], but the THz photons are not involved in the oscillation mechanism. This is in contrast to the optical Bloch gain observed in QCLs beyond the THz range [24], which has been forecast in Ref. [28]. The gain relies there upon stimulated emission of localized dipoles—rather than conduction currents—through a second-order photon-assisted mechanism, namely a transition involving both an electron and a photon and requiring transverse momentum exchange between initial and final states.

In Figs. 7 and 8, only the electrostatic retroaction J is increased in comparison to Fig. 5. One may conclude that Bloch oscillation instability only requires slightly higher values of J, i.e., of the charge density, than in the present samples. Preliminary experimental results indicate that increasing doping of all wells homogeneously by a factor of two is not compatible with the bistability regime however, nor is the repetition of two basic patterns of the structure. It is thus necessary to design appropriate doping profiles in the injectors and the superlattice portions to improve charge transfer at equilibrium and get better control of electrostatic retroaction in order to reach nonlinear Bloch oscillations, especially in thicker structures than in the present work.

V. CONCLUSION

In conclusion, combined nearest and next-nearest neighbor tunnel injection into a biased superlattice gives rise to charge density and voltage bistability thanks to competition between two coherent conduction channels. Electrical characterizations of suitably designed superlattice structures give experimental support to the effect semiquantitatively. As injection is coherent, phase relations are established between the superlattice eigenstates. Above a threshold value, electrostatic retroaction provides a suitable nonlinear feedback for the steady generation of undamped spontaneous Bloch oscillations, locally nearby the injector. The present results unveil a picture of the dynamics of Bloch oscillations in a semiconductor superlattice in which the oscillatory regime can be driven by out of equilibrium coherence and sustained by electrostatic nonlinearity mainly based on retroaction of coherent injection onto the coherence oscillation frequencies.

ACKNOWLEDGMENTS

The authors acknowledge support by the French Agence Nationale de la Recherche through the ROOTS project and by the French RENATECH network. They are very grateful to Ulf Gennser for a critical reading of the manuscript.

APPENDIX A: ELECTROSTATIC RETROACTION

For negative field F in the bulk of the superlattice (see Figs. 1 and 2), the slope of the conduction band is given by

$$-e\frac{dV}{dx} = e\left(F + \frac{en_s}{\varepsilon}\delta\rho_{22}\right) \tag{A1}$$

and

$$-e\frac{dV}{dx} = e\left(F + \frac{en_s}{\varepsilon}[\delta\rho_{22} + \delta\rho_{11}]\right) \tag{A2}$$

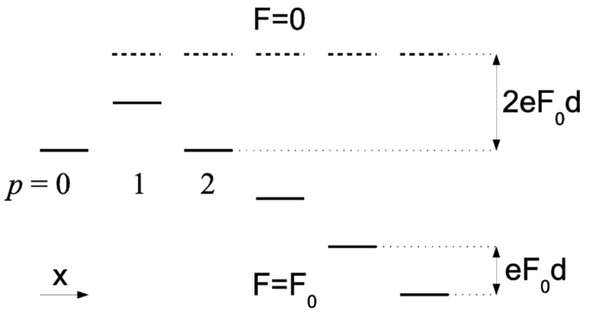

FIG. 9. Diagram of the unperturbed ground energy levels used in the transport model at zero field (dotted lines) and design field (solid lines).

between wells 1 and 2 and wells 0 and 1, respectively, where $\delta\rho_{pp} = \rho_{pp} - \eta_0$ and η_0 is the background doping in the superlattice.

Neglecting the perturbation of the eigenstates by the field changes, the energy shifts at $x = 2d$, $x = d$, and $x = 0$ are

$$-e\delta V_{|x=2d} = 0, \tag{A3}$$

$$-e\delta V_{|x=d} = -eFd - \frac{e^2 n_s d}{\varepsilon}\delta\rho_{22}, \tag{A4}$$

$$-e\delta V_{|x=0} = -2eFd - \frac{e^2 n_s d}{\varepsilon}(2\delta\rho_{22} + \delta\rho_{11}). \tag{A5}$$

In the transport model, Hamiltonian H_0 is only used to compute the electronic properties of the heterostructures at or close to the design electric field F_0. Then, the field dependence of the energy levels—Wannier-Stark ladder and injector levels—is assumed to be linear. Denoting ε_p the energy of state p, the energy differences are

$$\varepsilon_1 - \varepsilon_2 = -eFd - \frac{e^2 n_s d}{\varepsilon}\delta\rho_{22}, \tag{A6}$$

$$\varepsilon_0 - \varepsilon_2 = -2e(F - F_0)d - \frac{e^2 n_s d}{\varepsilon}(2\delta\rho_{22} + \delta\rho_{11}), \tag{A7}$$

$$\varepsilon_0 - \varepsilon_1 = -e(F - 2F_0)d - \frac{e^2 n_s d}{\varepsilon}(\delta\rho_{22} + \delta\rho_{11}). \tag{A8}$$

At equilibrium ($F = 0$), state $p = 0$ is shifted by $2eF_0 d$ with respect to the middle of the superlattice miniband, the energy where all Wannier-Stark states are assumed to converge to in the zero field limit (see Fig. 9).

APPENDIX B: COHERENT TRANSPORT EQUATIONS

Using the reduced field detuning parameter $\delta f = (F - F_0)/F_0$ and positive fields, the Liouville equation (4) [21] yields the full set of coherent transport equations:

$$\begin{aligned} i\frac{\partial\rho_{21}}{\partial t} &= -(1 + \delta f - J[\rho_{22} - \eta_0] + ir_3)\rho_{21} \\ &\quad + (1 + \delta f)u\rho_{01} - (1 + \delta f)v\rho_{20} + ir_3\overline{\rho}_{21} \\ &\quad - \frac{J'}{1 + \delta f}[\rho_{22} - \eta_0](\rho_{11} - \rho_{22}), \end{aligned} \tag{B1}$$

$$\begin{aligned} i\frac{\partial\rho_{00}}{\partial t} &= (1 + \delta f)u(\rho_{20} - \rho_{02}) + (1 + \delta f)v(\rho_{10} - \rho_{01}) \\ &\quad - i\frac{\rho_{00} - \overline{\rho}_{00}}{\tau_1} + i\frac{\rho_{00}^{22} - \overline{\rho}_{00}^{22}}{\tau_2}, \end{aligned} \tag{B2}$$

$$\begin{aligned} i\frac{\partial\rho_{20}}{\partial t} &= -(2\delta f - J[2\rho_{22} + \rho_{11} - 3\eta_0] + ir_2)\rho_{20} \\ &\quad - (1 + \delta f)v\rho_{21} + (1 + \delta f)u(\rho_{00} - \rho_{22}) + ir_2\overline{\rho}_{20} \\ &\quad - \frac{J'}{1 + \delta f}[\rho_{22} - \eta_0]\rho_{10}, \end{aligned} \tag{B3}$$

$$\begin{aligned} i\frac{\partial\rho_{22}}{\partial t} &= (1 + \delta f)u(\rho_{02} - \rho_{20}) - i\frac{\rho_{22} - \overline{\rho}_{22}}{\tau_1} \\ &\quad - \frac{J'}{1 + \delta f}[\rho_{22} - \eta_0](\rho_{12} - \rho_{21}), \end{aligned} \tag{B4}$$

$$\begin{aligned} i\frac{\partial\rho_{10}}{\partial t} &= (1 - \delta f - J[\rho_{22} + \rho_{11} - 2\eta_0] - ir_1)\rho_{10} \\ &\quad - (1 + \delta f)u\rho_{12} + (1 + \delta f)v(\rho_{00} - \rho_{11}) + ir_1\overline{\rho}_{10} \\ &\quad - \frac{J'}{1 + \delta f}[\rho_{22} - \eta_0]\rho_{20}, \end{aligned} \tag{B5}$$

$$\begin{aligned} i\frac{\partial\rho_{11}}{\partial t} &= (1 + \delta f)v(\rho_{01} - \rho_{10}) - i\frac{\rho_{11} - \overline{\rho}_{11}}{\tau_1} \\ &\quad - \frac{J'}{1 + \delta f}[\rho_{22} - \eta_0](\rho_{21} - \rho_{12}). \end{aligned} \tag{B6}$$

In the vicinity of resonance, the initial density matrix is assumed to obey [11]

$$\overline{\rho}_{10} = \overline{\rho}_{20} = 0, \tag{B7}$$

$$\overline{\rho}_{12} = \frac{J_1\left(\frac{\Delta}{2k_B T}\right)}{N J_0\left(\frac{\Delta}{2k_B T}\right)} e^{-\frac{2eF_0 d}{k_B T}}, \tag{B8}$$

and $\overline{\rho}_{00} = 1$, $\overline{\rho}_{00}^{22} = 0$, $\overline{\rho}_{11} = \overline{\rho}_{22} = \eta_0$, where

$$\eta_0 = \frac{1}{N} e^{-\frac{2eF_0 d}{k_B T}}. \tag{B9}$$

In Eqs. (B1)–(B6), energies have been scaled on either side by the Bloch energy eFd at field $F = F_0$ and times by $T_{B_0}/2\pi$, so that u and v are coupling dipoles scaled by d, and r_1, r_2, r_3 the coherence relaxation rates of the Wannier-Stark states scaled by the Bloch angular frequency $\omega_{B_0} = 2\pi\nu_{B_0}$. τ_1 and τ_2 are scaled lifetimes for the ground states at each well and at the upper state in the injector, respectively. In Eq. (B8), J_1 and J_0 are Bessel functions of the first kind.

The present model does not prevent the nonlinear response from transiently reaching unphysical values for strong deviations from the static regime because the contact layers and their quasi-Fermi levels are not taken into account. Charge densities in the Wannier-Stark states may become negative especially when the background doping η_0 is weak. Noting that the energy barrier for electron injection is reduced from $\Delta\varepsilon_e = 2eF_0 d$ to $\Delta\varepsilon_r = eF_0 d$ when the electric field is increased from its equilibrium value $F = 0$ to its value in the vicinity of resonance $F \sim F_0$, the background doping is taken as $(1/N)e^{-\Delta\varepsilon_r/k_BT}$ with $N = 5$ in Eqs. (B8) and (B9)—a value equal to η_0 for $N = 2$ when $k_BT \sim 11$ meV. As the model does not take subband filling into account, the thermal energy k_BT is considered to remain a constant equal to 10 meV, for the electronic temperature is expected to be larger than the lattice temperature in the vicinity of resonance due to carrier relaxation and heating effects in the transverse directions. Finally, fast population relaxation from the ground state is assumed with $\tau_1 = 1.5$ in order to avoid too strong damping of the nonlinear dynamics, although this overestimates the reference current in comparison with the experiments in the static regime.

---

[1] F. Bloch, Z. Phys. **52**, 555 (1928).
[2] L. Esaki and R. Tsu, IBM J. Res. Dev. **14**, 61 (1970).
[3] J. Feldmann, K. Leo, J. Shah, D. A. B. Miller, J. E. Cunningham, T. Meier, G. von Plessen, A. Schulze, P. Thomas, and S. Schmitt-Rink, Phys. Rev. B **46**, 7252 (1992).
[4] K. Leo, P. Haring Bolivar, F. Brüggemann, R. Schwedler, and K. Köhler, Solid State Commun. **84**, 943 (1992).
[5] C. Waschke, H. G. Roskos, R. Schwedler, K. Leo, H. Kurz, and K. Köhler, Phys. Rev. Lett. **70**, 3319 (1993).
[6] T. Dekorsy, P. Leisching, K. Köhler, and H. Kurz, Phys. Rev. B **50**, 8106 (1994).
[7] G. H. Wannier, Rev. Mod. Phys. **34**, 645 (1962).
[8] M. Glück, A. R. Kolovsky, H. J. Korsch, and F. Zimmer, Phys. Rev. B **65**, 115302 (2002).
[9] J. F. Palmier, C. Minot, J. L. Lievin, F. Alexandre, J. C. Harmand, J. Dangla, C. Dubon-Chevallier, and D. Ankri, Appl. Phys. Lett. **49**, 1260 (1986).
[10] A. Sibille, J. F. Palmier, H. Wang, and F. Mollot, Phys. Rev. Lett. **64**, 52 (1990).
[11] C. Minot, Phys. Rev. B **70**, 161309 (2004).
[12] H. Eisele, S. P. Khanna, and E. H. Linfield, Appl. Phys. Lett. **96**, 072101 (2010).
[13] P. Guéret, Phys. Rev. Lett **27**, 256 (1971).
[14] B. W. Knight and G. A. Peterson, Phys. Rev. **155**, 393 (1967).
[15] P. G. Savvidis, B. Kolasa, G. Lee, and S. J. Allen, Phys. Rev. Lett. **92**, 196802 (2004).
[16] E. Schomburg, R. Scheuerer, S. Brandl, K. F. Renk, D. G. Pavel'ev, Yu. Koschurinov, V. Ustinov, A. Zhukov, A. Kovsh, and P. S. Kop'ev, Electron. Lett. **35**, 1491 (1999).
[17] C. Minot, N. Sahri, H. Le Person, J. F. Palmier, J. C. Harmand, J. P. Medus, and J. C. Esnault, Superlattices and Microstructures **23**, 1323 (1998).
[18] S. M. Sze, *High-Speed Semiconductor Devices* (Wiley, New York, 1990).
[19] J. Kastrup, R. Hey, K. H. Ploog, H. T. Grahn, L. L. Bonilla, M. Kindelan, M. Moscoso, A. Wacker, and J. Galan, Phys. Rev. B **55**, 2476 (1997).
[20] M. Patra, G. Schwarz, and E. Schöll, Phys. Rev. B **57**, 1824 (1998).
[21] R. F. Kazarinov and R. A. Suris, Fiz. Tekhn. Poluprov. **6**, 148 (1972) [Sov. Phys. Semicond. **6**, 120 (1972)].
[22] J. Faist, F. Capasso, D. L. Sivco, C. Sirtori, A. L. Hutchinson, and A. Y. Cho, Science **264**, 553 (1994).
[23] B. S. Williams, Nat. Photonics **1**, 517 (2007); C. Sirtori, S. Barbieri, and R. Colombelli, *ibid.* **7**, 691 (2013).
[24] R. Terazzi, T. Gresch, M. Giovannini, N. Hoyler, N. Sekine, and J. Faist, Nat. Phys. **3**, 329 (2007).
[25] S. A. Ktitorov, G. S. Simin, and V. Ya. Sindalovskii, Fiz. Tverd. Tela **13**, 2230 (1971) [Sov. Phys. Solid State **13**, 1872 (1972)].
[26] A. A. Ignatov, E. P. Dodin, and V. I. Shashkin, Mod. Phys. Lett. B **5**, 1087 (1991).
[27] N. Sekine and K. Hirakawa, Phys. Rev. Lett. **94**, 057408 (2005).
[28] H. Willenberg, G. H. Döhler, and J. Faist, Phys. Rev. B **67**, 085315 (2003).
[29] The Bloch oscillator is considered herein as a purely electronic device. Coupling to the THz electromagnetic field is neglected and is considered to occur in a load circuit. Assessments of coupling in an active antenna can be found in Ref. [33].
[30] C. Minot and V. S. Jagtap, French patent 2980642-A1 (2013).
[31] P. England, M. Helm, J. R. Hayes, J. P. Harbison, E. Colas, and L. T. Florez, Appl. Phys. Lett. **54**, 647 (1989).
[32] C. Zhang, M. L. F. Lerch, A. D. Martin, P. E. Simmonds, and L. Eaves, Phys. Rev. Lett. **72**, 3397 (1994).
[33] V. S. Jagtap and C. Minot, IEEE Trans. Terahertz Sci. Technol. **2**, 131 (2012).
[34] R. Ferreira, P. Voisin, and G. Bastard, Solid-State Electron. **37**, 857 (1994).
[35] S. Kumar, B. S. Williams, Q. Hu, and J. L. Reno, Appl. Phys. Lett. **88**, 121123 (2006).
[36] G. Bastard, IEEE J. Quantum Electron. **22**, 1625 (1986).
[37] C. Minot, Phys. Status Solidi C **4**, 347 (2007).
[38] AUTO continuation software, http:/indy.cs.concordia.ca/auto/.
[39] A. W. Ghosh, L. Jönsson, and J. W. Wilkins, Phys. Rev. Lett. **85**, 1084 (2000).